CONDENSED-STATE PHYSICS

STRUCTURE FORMATION OF COMPOSITE MATERIAL BASED ON FERRITE-PEARLITE STEEL AND ALUMINUM BRONZE PRODUCED BY WIRE-FEED ELECTRON BEAM ADDITIVE MANUFACTURING

A. V. Chumaevskii, K. S. Osipovich, A. O. Panfilov,
A. M. Cheremnov, A. V. Vorontsov, N. L. Savchenko,
D. A. Gurianov, S. Yu. Nikonov, and E. A. Kolubaev

UDC 538.911: 621.521: 538.951

The features of structure formation and properties of bronze-steel composite samples formed by wire-feed electron beam additive manufacturing are studied. The studies show that at the bronze-to-steel ratio of 1:1 quite homogeneous structure is formed in them, with dendritic steel fragments and bronze filling the interdendritic space. When fabricated at the optimum process parameters, the samples do not contain any pores, inclusions, discontinuities or delamination. The strength characteristics of the resulting composites significantly exceed those of the base pure bronze. The mechanical properties of the samples are very similar in the compression and build direction. The yield strength values, calculated based on the contributions from different phases, differ from the measured values by up to 20%.

Keywords: composite materials, ferrite-pearlite steel, aluminum bronze, microstructure, mechanical properties, microstresses, electron beam manufacturing.

INTRODUCTION

With a rapid advancement of technologies and industrial development, there is an increasing need for materials with complex properties in different parts of a product. Therefore, it is necessary to develop materials with superior multiple properties for use in industrial production. By combining materials with different properties, new composites can be manufactured, which combine their advantages. Many researchers [1, 2] are focusing on various new methods and technologies for designing composite materials with superior mechanical properties. Some of the defining criteria for the materials in the present-day world are high strength, electrical conductivity and corrosion resistance, as well as zero material brittleness. In view of this, there is an increasing demand for bronze- and steel-based composite materials. Bronze products are used in various industries: instrumentation, marine, construction, engineering, etc. Bronze is used in the manufacture of products requiring high antifriction properties, in the manufacture of mechanisms in the chemical industry, and in the manufacture of high-precision equipment. Such a wide range of practical applications is due to its high corrosion resistance and strength, melting point of 1060°C, hot working temperature within 750–850°C, and annealing temperature in the range of 650–750°C. An unquestionable advantage of the ferrite-pearlite steel is its zero brittleness and a decreased level of toughness after a temperature exposure. This property distinguishes A516 steel among other representatives of this class with a high content of various alloying additions or carbon, due to which after heat treatment their properties cardinally change and the weldability deteriorates. Simply put, there are no standard side

effects generally manifested by a sharp decrease in the level of steel ductility or grain size of the composite. This steel is used in construction and mechanical engineering for the production of structural and connecting elements and parts subjected to high loads in a wide range of temperatures. Traditionally, hot and cold rolling of metal plates, tubes and sheets [3] or explosion welding/plating [4] have been used to produce large-volume bimetallic parts on an industrial scale. Additive manufacturing – a technology for forming products by selective melting or direct deposition of materials using the arc, laser or electron beam wire-feed processes, makes it possible to produce complex and/or miniature bimetallic parts [5]. Steel- and bronze-based composite materials are widely used as bearings and heat exchangers in the automotive industry [6]. Numerous recent studies [7–9] have addressed various aspects of the characteristics of interfacial interaction between the copper (bronze)-based bimetallic materials and the iron (steel)-based bimetallic materials produced by additive manufacturing. For instance, Tan et al. [7] investigated the interfacial characteristics and mechanical properties of a martensitically-aging functional steel-copper bimetal produced by selective laser melting in the course of a hybrid process. They observed the formation of microcracks at the interface, which propagated within the materials due to residual stresses caused by differences in thermal conductivity and thermal expansion coefficients and responsible for the interface discontinuities. Chen et al. [9] investigated the interfacial microstructure and mechanical properties of a 316L/CuSn10 multicomponent bimetal fabricated by selective laser melting. The authors also observed microcracks at the interface between the metallic parts and attributed them to the thermal conductivity mismatch between the materials. However, when these composites with the components additively grown on one side operate in a marine environment, a potential difference develops at the interface of the bimetallic structure, causing severe couple corrosion. The rest of the steel substrate remains exposed to the environment and the performance of the composite structure is significantly deteriorated. Furthermore, the research on the nickel-aluminum-bronze/steel composite structures is still limited to the pre-forming process and microstructure studies; its specific properties and corresponding failure behavior have not yet been systematically addressed [10]. The purpose of this study is to establish the relationship between the structure and mechanical properties of a composite material based on ferrite-pearlite steel and aluminum bronze fabricated by wire-feed electron beam additive manufacturing.

MATERIALS AND METHODS

The experimental composite samples were manufactured by the electron beam 3D printing, using the A516 low-carbon steel and CuAl9Mn2 tin-free bronze wires and a SS321 stainless steel plate as a substrate. The steel and bronze wires had the same diameter of 1.6 mm. An electron beam was used to form a melt pool in a vacuum chamber on the substrate, which was mounted on a three-axis water-cooled moving table, and the steel and bronze wires were simultaneously and continuously fed into the electron beam focus.

When dissimilar wires are used, such thermal conditions are created during printing where the steel wire does not have the time to melt and the bronze wire material excessively flows when melted. The beam current in our case was 72.5 mA at the beginning and 43.75 mA at the end of printing. The printing rate was 400 mm/min.

In order to reveal the structure for the light microscopy studies, the samples were chemically etched in a solution of 60 ml HCl + 10 g $FeCl_3$ + 120 ml H_2O. The macrostructural studies were performed with an Olympus LEXT confocal microscope (Olympus NDT, Inc., Waltham, MA, USA). The microstructural studies were performed using a LEO EVO 50 scanning electron microscope (Zeiss, Germany). Samples were cut from the grown vertical walls according to the scheme given in Fig. 1 using a DK7750 electric discharge machine to form test pieces for the study of the structure and mechanical properties. The tensile test pieces with a gaging area of $12 \times 2.5 \times 2.7$ mm^3 were used to study the mechanical properties. The tests were performed on a UTS 110M universal testing machine (Testsystems, Ivanovo, Russia). The strain rate was $1.4 \cdot 10^{-3}$ s^{-1}. The tests were performed on samples cut in the vertical (building direction) and horizontal (printing trajectory) directions.
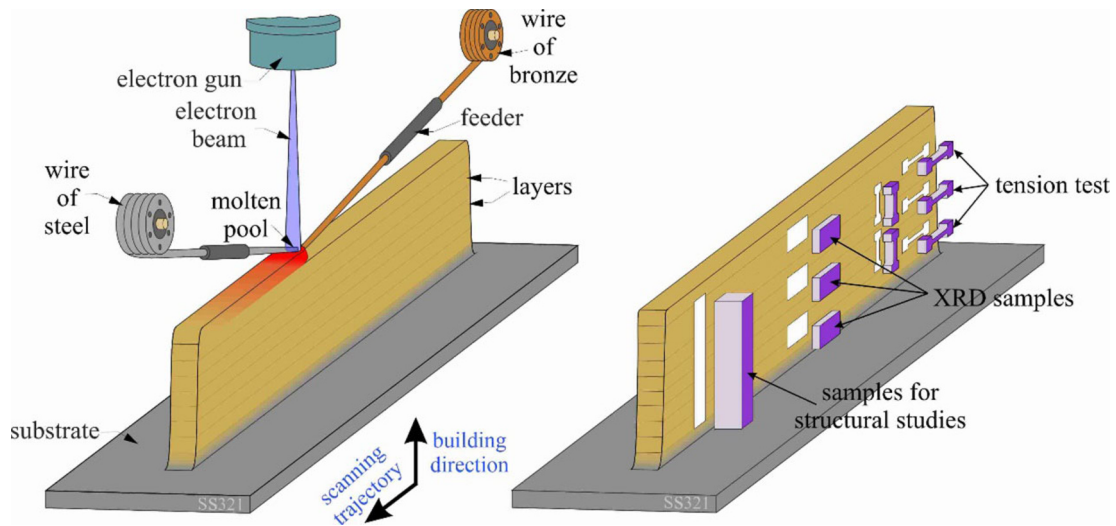
Fig. 1. Scheme of cutting samples into metallographic sections and samples for mechanical testing.

RESULTS AND DISCUSSION

Figure 2 shows a panoramic image of the longitudinal section of the composite sample with an equal volume ratio of dissimilar materials (bronze and steel). When the first layer is deposited, the substrate melts under the electron beam influence. At the same time, in the top part of the substrate, the deposited dissimilar materials are mixed with the substrate material with a simultaneous feed of the wire. The depth of penetration into the substrate is determined by changing the printing parameters when subsequent layers are applied. During the layer-by-layer deposition, the electron beam melts the fed wire, forming a melt pool, and penetrates through the substrate: the traces of circulation currents caused by the Marangoni effect can be seen. Since the Marangoni thermal convection positively depends on the surface tension and the temperature gradient, the presence of water cooling of the 3D printing table and the use of aluminum bronze, which has a higher thermal conductivity compared to steel, increase the depth of penetration into the substrate [11]. Utyaganova et al. [12] and Son et al. [13] experimentally showed that the use of a high heat input is required to form a high-quality layer on the substrate. In this work, the heat input value was calculated using the following formula [12]:

$$Q = (60*U*I)/(1000*v), \tag{1}$$

where U and I are the electron beam voltage and current, v is the printing rate. Using the printing parameter data (Table 2) and formula (1), we obtained the dependence of the layer-by-layer heat input (Fig. 3). After the formation of the lower layers, the value of the heat input decreases exponentially and printing is carried out with less intensive heating of the material, as a result of which the upper layers are not excessively overheated and the depth of penetration into the substrate is reduced.

The difference in thermal conductivity between the deposited dissimilar materials and the substrate leads to the formation of a pore-like defect, without any delamination of the deposited layer or the substrate. The difference in physical properties results in a temperature gradient that reduces the influence of the water-cooled table. In the finished product, this area is further removed and plays but an accidental role in practical applications.

The presence of the temperature gradient also affects the droplet fractions of dissimilar materials in the samples. When bronze and steel wires are fed simultaneously, thermal conditions are created in which the steel wire does not have time to melt due to the excessive heat dissipation caused by the bronze material fed into the melt pool.
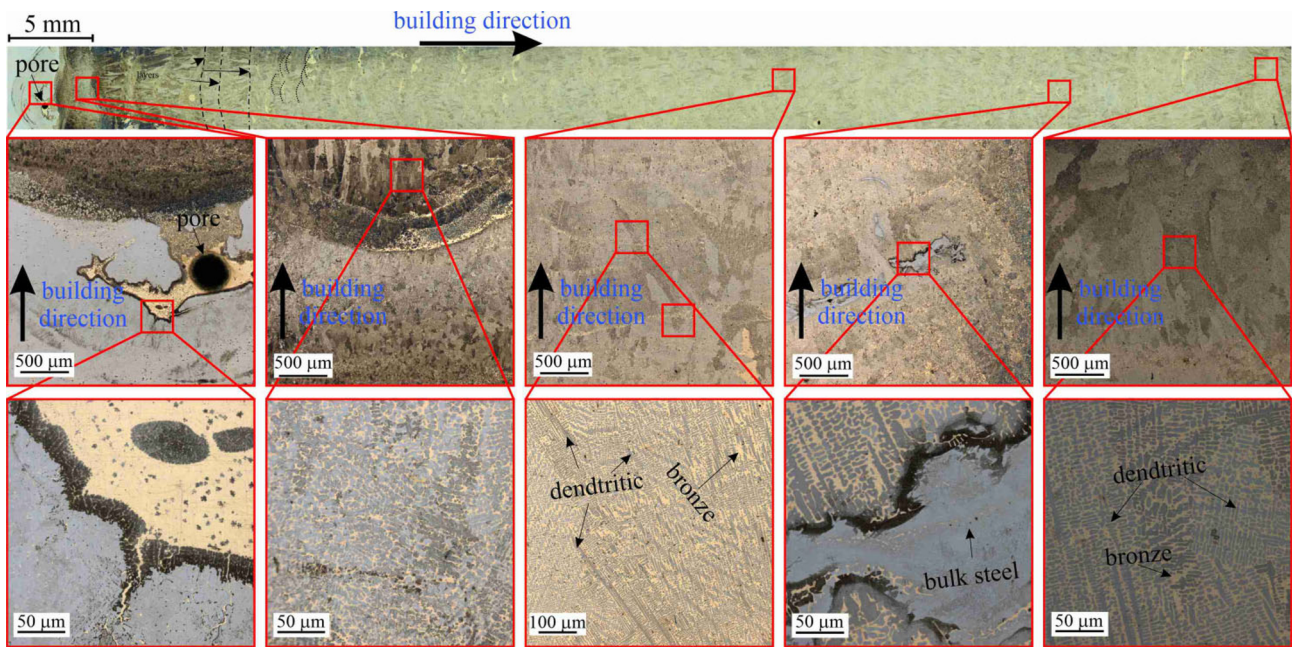
Fig. 2. Panoramic image of the longitudinal section of a composite material sample based on ferrite-pearlite steel and aluminum bronze, produced by wire-feed electron beam additive manufacturing. The bottom-row presents the magnified images corresponding to the interface between the first layer and the substrate, and the bottom, middle and top parts of the sample.

Typical characteristics are observed in additively manufactured products in the cases where overlapping semi-elliptical molten pools are formed. The melt boundaries in the sample can be seen as *fish scales* filled with a cellular structure [14]. As the upper layer expands, it is confined by the much colder lower layer, causing elastic compressive deformation. At elevated temperatures, however, the yield strength of the upper layer decreases, allowing plastic compressive deformation. Cooling of the now plastically compressed top layer causes it to shrink, inducing a bending angle with respect to the electron beam. This results in tensile stresses in the build direction. It is important to note that this mechanism occurs in the solid phase (and does not require melting of the material) [15]. Due to this effect, it is possible to notice a change in the size of the structural elements within a single layer: from equiaxed to small elongated grains. This feature is observed only in the lower part of the sample. It is worth noting that not only the general shape of the boundaries of the melt pool is archwise, but also the occasional unmelted regions of dissimilar materials, where successively solidifying metal droplets also form an arcuate interface under the surface tension. Since the electron beam additive process is a layer-by-layer deposition of a material to manufacture a product, there is a constant remelting of the deposited layers, or thermocycling. Thermocycling leads to an evolution of the structure in terms of its height in separate zones: bottom, middle and top parts of the sample. This implies an increase in the spacing between the primary dendrite arms and growth of the secondary dendrite arms. This is accounted for by the thermal energy provided by the high-power electron beam, which can to some extent reduce the solidification rate, thus giving the dendrite more time to grow during solidification. It has been observed that the development of crystallization cells is associated with the segregation of alloying elements at the cell boundaries leading to micro-segregation, which has also been observed in LPBF martensitic steels [16]. The dendritic structure mainly developed in the direction slightly differing from the building direction (z) due to the heat gradient variations during solidification. The grain growth direction can be closely related to the building direction, especially in the electron beam wire-feed additive manufacturing, where the electron-beam scanning speed is high [17].

It can be clearly seen that the sample has a homogeneously solidified microstructure, with dark iron-rich dendrites uniformly and randomly embedded in the copper matrix over the entire height without large-scale segregation or spatial phase separation. Comparing the structure in the central and upper parts of the sample (Fig. 3), one can see
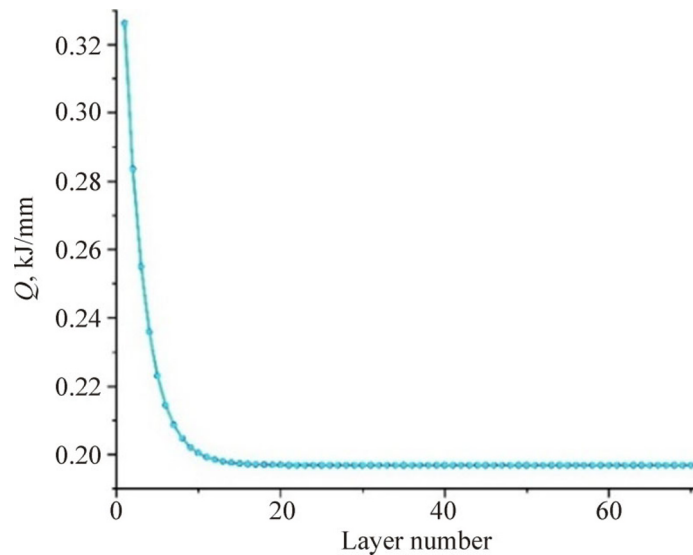
Fig. 3. Variation of heat input during layer-by-layer printing of composite
material based on ferrite-pearlite steel and aluminum bronze.

that thermal cycling significantly affects the morphology and size of the iron-enriched dendrites. In the central part of the sample, the morphology of the iron-enriched phase is predominantly represented by finely-meshed dendrites. In the upper part of the sample, the morphology clearly changes from fine dendrites to cellular dendrites and to well-developed dendrites.

After the formation of a homogeneous melt, the bronze-steel alloy in the present experiment cannot reach a high enough degree of supercooling to enter the metastable interval of miscibility, so a liquid-solid equilibrium is established. Compared with the traditional manufacturing technology, the degree of segregation in our case is significantly lower. Since 3D printing can be regarded as a directional solidification process with a high temperature gradient and a high cooling rate, the elements located in the dendritic arms and interdendritic space diffuse rapidly, and the material composition distribution is more homogeneous than that in a conventional cast microstructure [18].

The common feature of this composite material is a fine-grained microstructure typical for high cooling rates. According to the content of heterogeneous components, we distinguish between an oriented and non-oriented structure. In the composite, one component plays the role of a matrix, which forms a continuous phase, and the other component – the role of a filler. According to Fig. 2, the primary dendrite arms are thin and the secondary dendrite arms are well developed in the upper part of the sample. However, in the upper part of the sample, the dendrites become finer and the spacing between the adjacent primary and secondary dendrite arms gradually decreases. During 3D printing, the lower part of the sample is heated for a longer period of time, and the solidified material can exert a quenching effect on the previous layers. The accumulated heat can provide enough energy for the dendrites to grow, even if they are developed and larger in size. However, in the upper part of the sample, dendrites solidified quickly, and the number of nucleating dendrites was large.

The mechanical properties of the samples cut in the growth and printing directions hardly differ (Fig. 4). The largest differences are observed in the sample plasticity. The scatter of the plasticity values of individual samples in the vertical direction is higher than that in the horizontal direction. At the same time, a three-stage stress-strain diagram is typical for the samples, including the sections of elastic deformation and two stages of plastic deformation with differing stress variation intensity.

Micromechanical models of composites can reveal analytical relationships showing the influence of the matrix and filler properties, their interaction, and material structure. They are most successful in describing the yield strength of a composite. In the case where the filler and matrix deformations are equal, the following additive relationships are obtained, showing the contribution of each component in proportion to its volume content [19]:

TABLE 1: Mechanical Properties of Composite Material based on Bronze and Steel in 1:1 Ratio

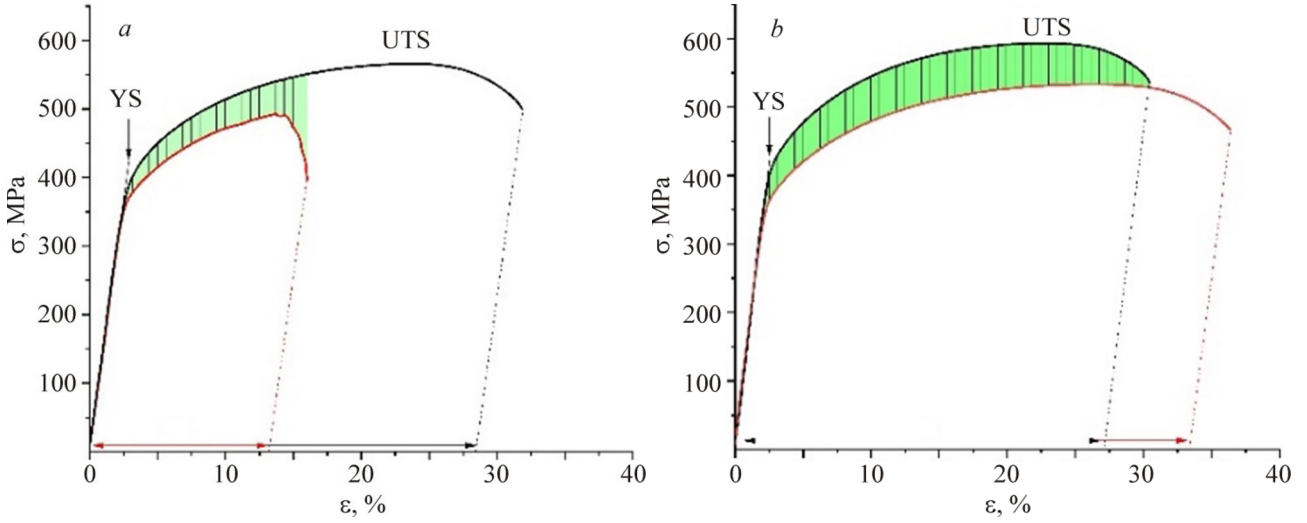| Mechanical properties	Strength properties	
	Printing direction	Building direction
YS, MPa	371	361
UTS, MPa	562	538
ε, %	30	25
σ_{YS}^{K}, MPa	299	297

Fig. 4. The σ-ε curves for vertically (*a*) and horizontally (*b*) cut samples of ferrite-pearlite steel and aluminum-bronze composite material produced by wire-feed electron beam additive manufacturing.

$$\sigma_{YS}^{K} = \sigma_{YS}^{1} * \varphi_1 + \sigma_{YS}^{2} * \varphi_2, \tag{2}$$

where σ_{YS}^{1}, σ_{YS}^{2} are the yield strengths of ferritic-pearlitic steel and aluminum bronze, respectively, and φ_1, φ_2 are the volume fractions of heterogeneous materials in the composite. The tensile strength values for steel were determined experimentally by applying a uniaxial tensile load; for bronze we relied on our earlier work [20]. Using this formula, the theoretical yield strength for the composite was calculated (Table 1). The theoretical and experimental yield strengths differ, which can be explained by the presence of internal stresses.

Formula (3) was used to quantify the stress value of the two-phase material (α-Fe and Cu) [21]

$$\frac{d_{\Psi\varphi} - d_0}{d_0} = \left(\frac{1+\nu}{E} \right) \cdot \sigma_{\Phi} \cdot \sin^2(\Psi) \cdot (\sigma_1 + \sigma_2), \tag{3}$$

where E is the elasticity modulus of the material, ν is the Poisson's ratio of the investigated phase, d_0 is the interplanar distance in the unstressed state, $d_{\Psi\varphi}$ is the interplanar distance for the characteristic reflection planes perpendicular to the beam incidence direction (Ψ). This formula is used to determine the value of stresses in the plane of the sample surface in the direction φ.

TABLE 2. Residual Stress Values Calculated for $(331)_{Cu}$, $(222)_{\alpha-Fe}$ and $(420)_{Cu}$ Planes

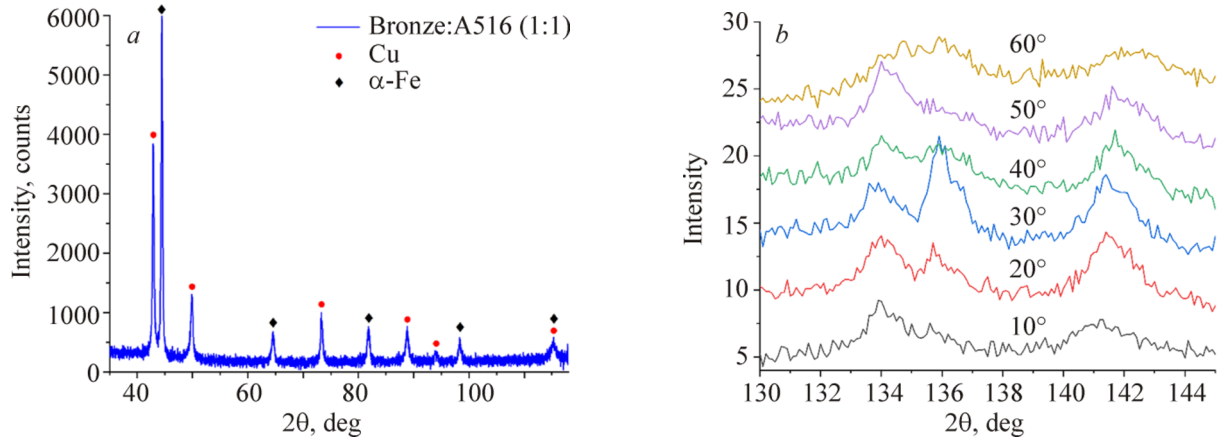| Reflection plane of analyzed phase	d_0, nm	Tilt angle of straight line i	Residual stresses, MPa
$(331)_{Cu}$	0.08364	−0.00832	−99.5
$(222)_{Fe}$	0.08306	−0.04548	−547.6
$(420)_{Cu}$	0.08124	−0.01002	−123.3

Fig. 5. Phase analysis of the X-ray profile of the Bronze:A516 composite sample (*a*) and a series of asymmetric X-ray patterns obtained at fixed angles Ψ from 10 to 60 degrees, indicated on the right, for every X-ray pattern (*b*).

Figure 5*a* is a primary X-ray pattern obtained using Bragg-Brentano focusing and showing X-ray for a 1:1 composite (bronze : steel A516). This composite is a two-phase material consisting of an FCC copper lattice and a BCC iron lattice.

A symmetrical imaging was performed to determine the position of the $2\theta_0$ angles to identify the phases and the position of the α-Fe and Cu reflections. The (331) and (420) reflections were selected for the Cu FCC lattice and the (222) reflection was selected for the α-Fe lattice for the stress calculations. These reflections were chosen in order to reduce the error of the stress value measurements. It was difficult to overlap the $(331)_{Cu}$ and $(222)_{Fe}$ reflections having close angular positions $2\theta_0$ (134° and 135.8°).

After the identification of the analyzed Cu and α-Fe phase reflections, a series of asymmetric scans were made at the Ψ angles equal to 10–60° with a step of 10°. In Fig. 5*b* shows a group of asymmetric scans for $(331)_{Cu}$, $(420)_{Cu}$, $(222)_{\alpha-Fe}$ reflections in the range of 130–145° 2θ. The X-ray patterns were approximated by a standard Voigt function used in the X-ray diffraction analysis.

After determining the angular position of the reflections, as in [21], to analyze the residual stresses, a linear dependence in coordinates was taken as follows: $d_{\Psi\varphi} - \left(\dfrac{1+\nu}{E}\right)\cdot\sin^2(\Psi)\cdot\left(\dfrac{2\nu}{E}\right)$. The type of dependence for each analyzed reflex is shown in Fig. 6. Note that in the equation of the approximation line, the intersection with the ordinate axis of the line is the value d_0. The stress σ_φ is calculated as the ratio of the coefficient a of the straight line to the slope ratio of this straight line.

Finally we obtained the values of residual stresses calculated from the reflection planes of the two-phase materials $(331)_{Cu}$, $(222)_{\alpha-Fe}$ and $(420)_{Cu}$. The results of the analyzed values and the stress calculations are shown in Table 2.

In the data obtained in this study there is a very big difference between the stresses of different phases; on average the residual stresses for Cu are 111 MPa and for α-Fe − 547.6 MPa. In both cases, they are compressive.
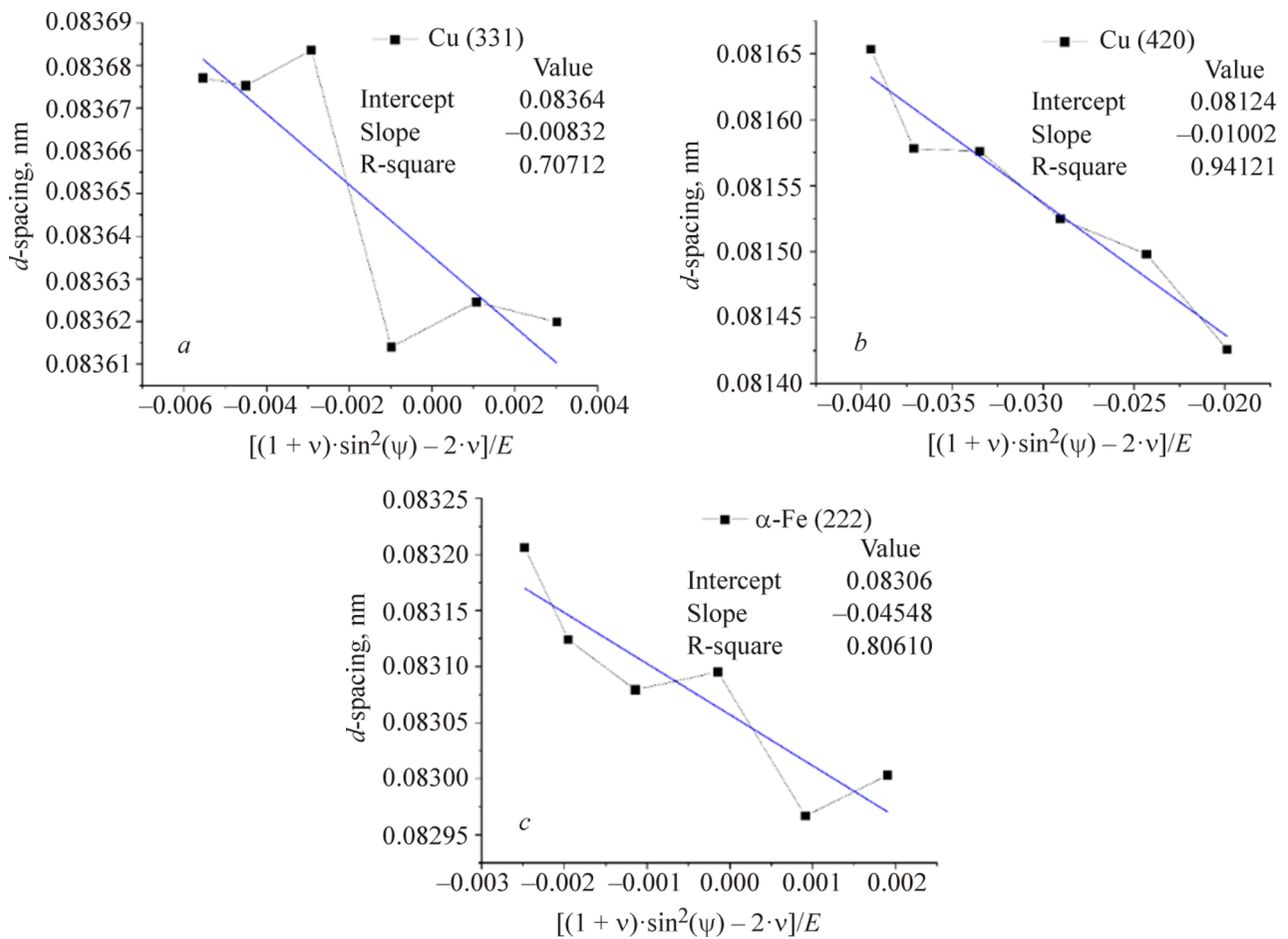
Fig. 6. Linear approximation of the dependence of the interplanar distance of the diffraction maxima of $(331)_{Cu}$, $(222)_{\alpha\text{-Fe}}$ and $(420)_{Cu}$ on the function $[(1 + \nu) \cdot \sin^2(\psi) - 2 \cdot \nu]/E$.

However, it is worth noting that the determined value of the stresses along the $(331)_{Cu}$ and $(222)_{\alpha\text{-Fe}}$ planes will have a larger error than that for (420)Cu due to close positions of the maxima. Therefore, it is logical to expect that the absolute average stress value, at least for the Cu-based phase of the printed composite, would be larger than 111 MPa.

CONCLUSIONS

The studies conducted in this work have shown a high applicability of the method of wire-feed additive electron beam printing for manufacturing the bimetallic composite materials based on aluminum-manganese bronze and steel in the component ratio of 1:1. The samples of composite structure, formed by printing under the conditions where two filaments are simultaneous fed directly of into the melt pool, are characterized by a homogeneous defect-free structure in the volume. Their mechanical properties are quite similar both in the printing and growth directions. The residual compressive stresses according to X-ray diffraction analysis are at a relatively high level, with the stresses being up to 5 times higher for the steel-based phase than those for the bronze-based phase. The mechanical properties (yield strength) of the samples exceed the values calculated from the available micromechanical models. This indicates that not only the phase ratio but also the phase structure and distribution in the bulk of the sample contribute to the values of this parameter.

COMPLIANCE WITH ETHICAL STANDARDS

Author contributions

A.C. and K.O., Conceptualization, Funding acquision, Investigation, Writing – Original Draft; A.P. and K.O., Methodology, Investigation, Data Curation, Vizualization; A.C., Methodology, Resources, Investigation; A.V., Investigation, Data Curation, Formal analysis; N.L. and S.N., Methodology, Resources; A.C. and A.C., Investigation, Data Curation, Formal analysis; E.K., Conceptualization, Writing – Review & Editing.

Conflicts of interest

The authors declare no conflict of interest.

REFERENCES

1. M. Hosseini, N. Pardis, H. D. Manesh, *et al*., Mater. Des., **113**, 128 (2017). https://doi.org/10.1016/j.matdes.2016.09.094.
2. N. V. Martyushev, I. V. Semenkov, Y. N. Petrenko, *et al*., Nanomater, 89 (2014). https://doi.org/10.4028/www.scientific.net/AMR.880.174.
3. G. P. Chaudhari and V. Acoff, Compos. Sci. Technol., **69**, 1667 (2009). https://doi.org/10.1016/j.compscitech.2009.03.018.
4. I. Hordych, K. Barienti, S. Herbst, *et al*., Metals, **11**, 917 (2021). https://doi.org/10.3390/met11060917.
5. E. S. Statnik, P. A. Somov, D. D. Zherebtsov, *et al*., Mater. Sci. Eng. A, **858**, 144110 (2022). https://doi.org/10.1016/j.msea.2022.144110.
6. I. N. Maliutina, V. I. Mali, I. A. Bataev, *et al*., Sci. World J., 256758 (2013). https://doi.org/10.1155/2013/256758.
7. C. Tan, K. Zhou, W. Ma, *et al*., Mater. Des., **155**, 77 (2018). https://doi.org/10.1016/j.matdes.2018.05.064.
8. E. A. Kolubaev, V. E. Rubtsov, A. V. Chumaevsky, *et al*., Phys. Mesomech., **25,** 479 (2022). https://doi.org/10.1016/j.jallcom.2018.01.318.
9. J. Chen, Y. Yang, C. Song, *et al*., Mater. Sci. Eng., A, **752**, 75 (2019). https://doi.org/10.1016/j.msea.2019.02.097.
10. X. Cai, Z. Wang, L. Dong, *et al*., Mater. Des., **221**, 110969 (2022). https://doi.org/10.1016/j.matdes.2022.110969.
11. S. Y. Tarasov, A. V Filippov, N. L. Savchenko, *et al*., Int. J. Adv. Manuf. Technol., **99**, 2353 (2018). https://doi.org/10.1007/s00170-018-2643-0.
12. V. R. Utyaganova, A. V. Filippov, N. N. Shamarin, *et al*., Int. J. Adv. Manuf. Technol., **108**, 2823 (2020). https://doi.org/10.1007/s00170-020-05539-9.

13. B. Song, X. Zhao, S. Li, *et al*., Front. Mech. Eng., **10**, 111 (2015). https://doi.org/10.1007/s11465-015-0341-2.

14. E. A. Jägle, P. P. Choi, J. Van Humbeeck, *et al*., J. Mater. Res., **29**, 2072 (2014). https://doi.org/10.1007/s11465-015-0341-2.

15. Y. Bai, Y. Yang, D. Wang, M. Zhang, Mater. Sci. Eng. A., **703**, 116 (2017). https://doi.org/10.1016/j.msea.2017.06.033.

16. V. Juechter, T. Scharowsky, R. F. Singer, *et al*., Acta Mater., **76**, 252 (2014). https://doi.org/10.1016/j.actamat.2014.05.037.

17. X. He, T. DebRoy, P. W. Fuerschbach, J. Appl. Phys., **94**, 6949–6958 (2003). https://doi.org/10.1063/1.1622118.

18. J. Zhou, J. Zhang, C. Hu, *et al*., Mater. Sci. Eng. A, **874**, 145088 (2023). https://doi.org/10.1016/j.msea.2023.145088.

19. Ya. B. Fridman, Mechanical Engineering [in Russian], Mashinostroyeniye, Moscow (1974).

20. A. Zykova, A. Panfilov, A. Chumaevskii, *et al.*, Mat. Lett., **338**, 108477 (2023). https://doi.org/10.1016/j.matlet.2023.134064.

21. Q. Luo and A. H. Jones, Surf. Coat. Technol., **205,** 1403–1408 (2010). https://doi.org/10.1016/j.surfcoat.2010.07.108.